Frontiers of Information Technology & Electronic Engineering
www.jzus.zju.edu.cn; engineering.cae.cn; www.springerlink.com
ISSN 2095-9184 (print); ISSN 2095-9230 (online)
E-mail: jzus@zju.edu.cn

Nonlinear programming control using differential aerodynamic drag for CubeSat formation flying*

Sheng-chao DENG†1, Tao MENG†‡2, Zhong-he JIN2
([1]College of Information Science and Electronic Engineering, Zhejiang University, Hangzhou 310027, China)
([2]School of Aeronautics and Astronautics, Zhejiang University, Hangzhou 310027, China)
†E-mail: dscsd0131@163.com; mengtao@zju.edu.cn

Received Dec. 31, 2015; Revision accepted Apr. 18, 2016; Crosschecked July 11, 2017

Abstract: Because of their volume and power limitation, it is difficult for CubeSats to configure a traditional propulsion system. Atmospheric drag is one of the space environmental forces that low-orbit satellites can use to realize orbit adjustment. This paper presents an integrated control strategy to achieve the desired in-track formation through the atmospheric drag difference, which will be used on ZJUCubeSat, the next pico-satellite of Zhejiang University and one of the participants of the international QB50 project. The primary mission of the QB50 project is to explore the near-Earth thermosphere and ionosphere at the orbital height of 90–300 km. Atmospheric drag cannot be ignored and has a major impact on both attitude and orbit of the satellite at this low orbital height. We conduct aerodynamics analysis and design a multidimensional nonlinear constraint programming (MNLP) strategy to calculate different desired area–mass ratios and corresponding hold times for orbit adjustment, taking both the semimajor axis and eccentricity into account. In addition, area–mass ratio adjustment is achieved by pitch attitude maneuver without any deployable mechanism or corresponding control. Numerical simulation based on ZJUCubeSat verifies the feasibility and advantage of this design.

Key words: QB50; ZJUCubeSat; Atmospheric drag; Formation flying
http://dx.doi.org/10.1631/FITEE.1500493 **CLC number:** TP2; V448.22

1 Introduction

CubeSat is a type of miniature satellite with special design standards, with the advantages of small volume, light weight, low power consumption, and low cost. CubeSats usually use ‘1U’ (a volume of 10 cm^3 and a mass of about 1 kg) as the measurement unit, and can be launched and deployed using a common deployment system. Driven by the increasing demand of distributed detection and in-orbit service, formation flying has been identified as the next revolutionary step in space technology. This trend drives the satellite to configure the orbit propulsion system and to have the capability of orbit maneuver. CanX-4&5 (Eyer *et al.*, 2007), designed by UTIAS/SFL, use a liquefied gas propulsion system with SF$_6$ as propellant. The ION-F project (Campbell *et al.*, 2000), an American University nano-satellite program, includes three nano-satellites and plans to use the pulsed plasma thruster, cold gas, and micro hydrazine propulsion, respectively. In 2006, three Space Technology-5 satellites (Lohn *et al.*, 2005), developed by NASA and configured with a high-pressure nitrogen micro-propulsion system, successfully formed a space constellation within 40–140 km to observe geomagnetic fields.

Although the propulsion system can help achieve high accuracy and variable formation constellations, it requires a relatively large volume and

---

‡ Corresponding author

* Project supported by the National Science Fund for Distinguished Young Scholars of China (No. 61525403) and the National Natural Science Foundation of China (No. 61503334)

ORCID: Sheng-chao DENG, http://orcid.org/0000-0002-4864-7984 relatively high power consumption. Besides, the propellant is limited and available only for a short period. These drawbacks pose many obstacles to configure a micro-propulsion system for CubeSats. Hence, researchers have begun to seek several alternative resources to realize orbit adjustment. Atmospheric drag is typically seen as an adverse factor, but it also brings a propellant-less solution for planning a formation flying mission.

In the prior work of Leonard *et al.* (1989), the formation dynamics was decoupled through differential atmospheric drag to a long-term double integral system and a periodic harmonic vibration. Reid and Misra (2011) analyzed the effects of atmospheric drag on the relative orbit and derived a recursive state space matrix under J2 perturbation. Lambert *et al.* (2012) evaluated several methods to estimate the mean relative motion state for the implementation of formation flying. Pérez and Bevilacqua (2013) designed an adaptive Lyapunov controller to adjust the relative orbit by driving several rotatable panels connected on the satellite.

Among the existing works, the phase plane method is the most commonly used one for atmospheric drag adjustment. This method sets a fixed altering size of cross-sectional area and then adjusts the relative orbit into a desired configuration through Bang-Bang (BB) switch control after at least one switch. However, the influence of the atmospheric drag on orbit eccentricity will increase the radial oscillation during the formation control period. Several researchers have considered radial and in-track oscillations simultaneously and chosen an appropriate start time to change the cross-sectional area, which can decrease the radial oscillation. However, it takes a long time to reach the final formation, and hundreds of meters of formation baseline might be required for a couple of days (Yao *et al.*, 2010). Furthermore, most studies have not taken the atmosphere's co-rotation with the Earth into consideration, which leads to the difference in the satellite's semimajor axes and an increase of in-track drifting with time. This will result in the final configuration being maintained for a very short time.

To put cross-sectional area adjustment into practice, Varma and Kumar (2012) achieved multiple satellite formation through sliding mode control and adjusted the cross-sectional area through rotatable solar panels symmetrically installed on the satellite. Pérez and Bevilacqua (2013) designed a closed-loop feedback Lyapunov control law to reach the configuration, comprehensively considering the effect of solar activity on the atmospheric thermal layer and adjusting the cross-sectional area with an expandable resistance sail fixed on the satellite's tail. Horsley *et al.* (2013) proposed that they could use a large panel connected to the satellite tail and decompose the atmospheric drag to the orbit plane normal by adjusting the angle of the panel, thereby achieving orbit-plane adjustment. These kinds of design are mostly based on expandable attachments on the satellite, including extensible flats, solar panels, and various kinds of sails. The cross-sectional area adjustment is calculated through different closed-loop control algorithms. Higher adjustment ability of a deployable structure can achieve a shorter reconfiguration time and a higher precision formation control. However, when it comes to smaller and lighter satellites, for instance, a 2U or 3U CubeSat, usually no deployable mechanism and no extra electric power can be supplied for the adjustment. Moreover, the control complexity and reliability of these appendages restrict their further application.

Based on the design constraints and orbital environment of the QB50 project, influence of the relative motion caused by the atmospheric drag is analyzed in this study. The multidimensional nonlinear constraint programming (MNLP) strategy is proposed to calculate different desired area–mass ratios and the corresponding hold times for orbit adjustment. Correspondingly, proportional–derivative (PD) control laws are designed for pitch attitude maneuver and three-axis attitude stabilization using a bias momentum wheel and magnetic coils, respectively. Thus, we can adjust the satellite cross-sectional area through pitch attitude fast maneuver to meet the orbit maneuver requirement without any deployable mechanism. Numerical simulations of both normal BB control and MNLP control are presented for comparison.

2 ZJUCubeSat overview

The QB50 project (Reinhard *et al.*, 2012) will demonstrate the possibility of launching a network of 50 CubeSats built by teams from universities all over the world to perform first-class science in the unexplored lower thermosphere. The purpose of the QB50 project is to establish an international network of 50 nano-satellites for multipoint, in situ measurements in the lower thermosphere and for reentry research.

As part of the QB50 project, ZJUCubeSat (Fig. 1) is a 2U CubeSat developed by the Microsatellite Research Center, Zhejiang University (ZJUMRC). It is an upgraded version of the ZDPS-1A satellite (Yang *et al.*, 2012), which was built by ZJUMRC and successfully launched in 2010. The main payload of ZJUCubeSat is a FIPEX Flux-Φ-Probe, designed and manufactured by TU Dresden, Germany, which is able to distinguish and measure the time-resolved behavior of atomic and molecular oxygen of the lower thermosphere. Besides, ZJUCubeSat carries three additional payloads: the inter-satellite ranging system, the GNSS receiver, and a digital camera Sun sensor. The inter-satellite ranging system will be used to conduct relevant in-orbit experiments with other QB50 CubeSats designed by Chinese universities.

Fig. 2 shows a general system configuration diagram of ZJUCubeSat. The attitude determination system (ADS) is composed of a three-axis gyro, a three-axis magnetometer (Cai *et al.*, 2011), three four-quadrant analog Sun sensors (Wang *et al.*, 2012) which are mounted on three illuminated surfaces ($-X$, $+X$, and $-Z$), and a digital camera Sun sensor mounted on the top surface for on-orbit verification. One momentum wheel is used for both providing bias momentum and maneuvering the pitch attitude. Three orthogonally mounted magnetic coils provide active control torque for detumbling and three-axis stabilization (Meng *et al.*, 2009). A TMS320C5747 series

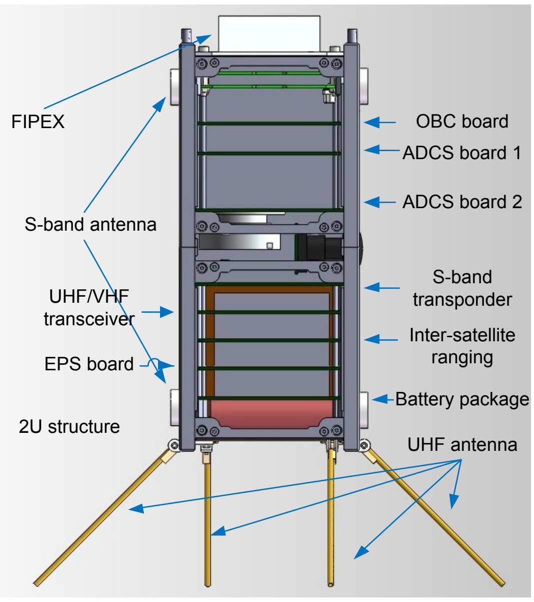

Fig. 1 ZJUCubeSat's configuration and hardware arrangement

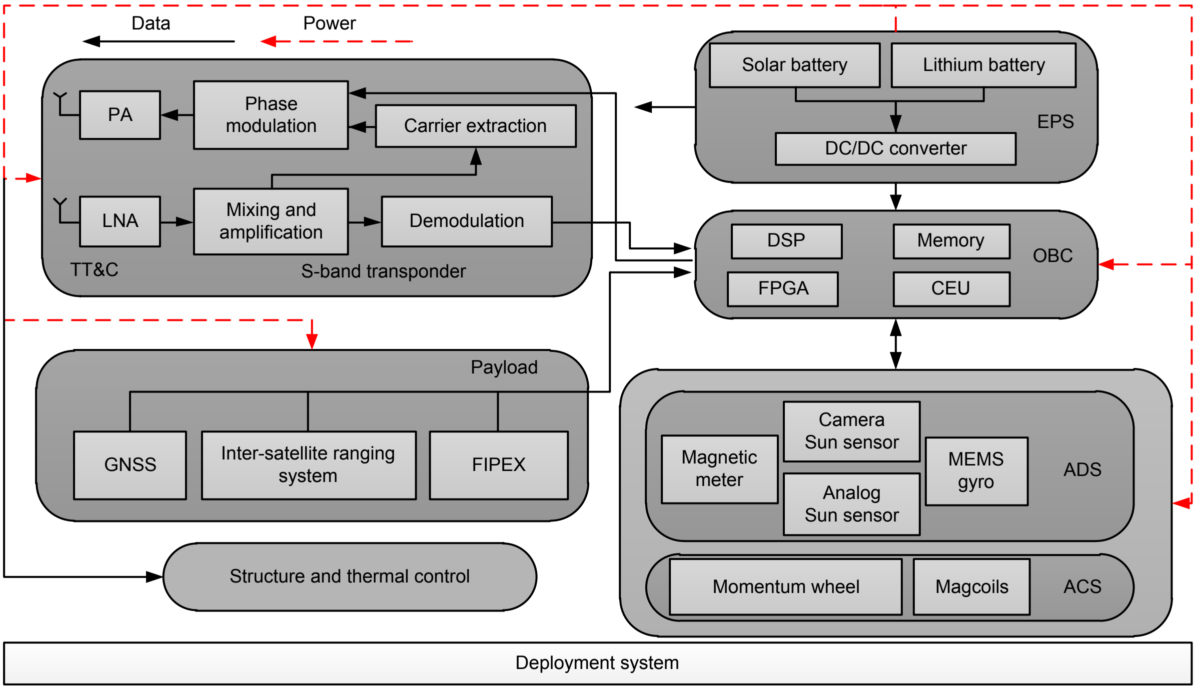

Fig. 2 ZJUCubeSat system configuration diagram

digital signal processor (DSP) is adopted as the main processor, and a Cool Runner II complex programmable logic device (CPLD) is used for interface expansion and data sampling.

Because of the great uncertainty of the initial orbit brought by the multiple satellite launch, relative distance and direction may not be able to meet the inter-satellite ranging experimental conditions. Thus, satellites need to have the ability for orbit maneuvering. However, the power supply is constrained by the CubeSat's standard structure, and it is difficult for a common propulsion system to meet such a small volume constraint. Hence, atmospheric drag is used to achieve the desired formation through cross-sectional area adjustment. The satellite attitude would be adjusted to meet the different area–mass ratio requirements. Considering the fact that atmospheric drag influences mainly the orbital plane motion, usually only in-track formation can be realized.

3 Aerodynamics analysis

3.1 Atmospheric drag acceleration

The acceleration brought by the atmospheric drag is generally estimated as follows (Montenbruck and Gill, 2012):

$$\boldsymbol{F}=-\frac{1}{2}C_{\mathrm{d}}\frac{A}{m}\rho\|\boldsymbol{v}\|\boldsymbol{v}, \tag{1}$$

where ρ is the atmospheric density, C_{d} is the satellite drag coefficient, which is generally taken as 2.0–2.2 for a cubic structure, A is the cross-sectional area, m is the mass of the satellite, and $\boldsymbol{v}$ is the satellite velocity vector relative to the atmosphere.

To facilitate the derivation, we assume that the atmospheric density decays exponentially with increasing altitude (Vallado, 2001):

$$\rho=\rho_0\exp\left(-\frac{r-r_0}{H}\right), \tag{2}$$

where ρ_0 is the nominal atmospheric density at a base altitude r_0 of a given altitude range, and H is called the scaled height for this given altitude range and can be obtained in the atmospheric model.

Atmospheric drag affects mainly the satellite's in-track motion and has little impact on the radial and normal motion. We define the orbital semimajor axis, eccentricity, inclination, right ascension of the ascending node, argument of perigee, mean anomaly, and true anomaly as a, e, i, Ω, ω, M, and f, respectively. Generally, the normal component of the force could be taken as zero. The radial and in-track components are given as follows (Reid and Misra, 2011):

$$\begin{cases} F_r=-\dfrac{\mu k\rho}{2p}e\sin f\cdot(1+2e\cos f+e^2)^{1/2}, \\ F_\theta=-\dfrac{\mu k\rho}{2p}(1+e\cos f)(1+2e\cos f+e^2)^{1/2}, \end{cases} \tag{3}$$

where μ is the gravitational parameter, $p=a(1-e^2)$, F_r and F_θ are the disturbing forces in the radial and in-track directions, respectively, and k is the drag coefficient, which will have a detailed description in the next step.

3.2 Gaussian atmospheric drag perturbation equations

Expressing the above formulae as Gaussian perturbation equations (Liu, 2000), we obtain the relationship between the atmospheric drag and orbital elements in Eq. (4), where E is the eccentric anomaly and $\mathrm{d}E/\mathrm{d}t=na/r$, n is the orbital angular rate, and $\mathrm{d}M^*/\mathrm{d}E$ is the variation of the mean anomaly introduced only by the atmospheric drag. $k=C_{\mathrm{d}}A/m$ if the atmosphere rotation is ignored, and $k=C_{\mathrm{d}}F^2A/m$ if it is considered, where $F=1-rn_{\mathrm{e}}\cos i/v\approx1-r_{\mathrm{p0}}n_{\mathrm{e}}\cos i/v_{\mathrm{p0}}$,

$$\begin{cases} \dfrac{\mathrm{d}a}{\mathrm{d}E}=-a^2k\rho(1+e\cos E)^{3/2}(1-e\cos E)^{-1/2}, \\ \dfrac{\mathrm{d}e}{\mathrm{d}E}=-a(1-e^2)k\rho(1+e\cos E)^{1/2}\cos E\cdot(1-e\cos E)^{-1/2}, \\ \dfrac{\mathrm{d}\omega}{\mathrm{d}E}=-a(1-e^2)^{1/2}e^{-1}k\rho(1+e\cos E)^{1/2}\sin E\cdot(1-e\cos E)^{-1/2}, \\ \dfrac{\mathrm{d}M^*}{\mathrm{d}E}=a(1-e^2)^{3/2}e^{-1}k\rho(1+e\cos E)^{1/2}\sin E\cdot(1-e\cos E)^{-1/2}[1+e^2(1-e^2)/(1-e\cos E)]. \end{cases} \tag{4}$$

r_{p0} and v_{p0} are the initial geocentric altitude and angular velocity of the perigee, respectively, and n_e is the rotation angular velocity of the Earth.

For a nearly circular orbit, we can assume that the atmospheric density is constant. Integrating Eq. (4) for one orbit cycle, the variation of the orbit elements is obtained as

$$\begin{cases} \Delta a = \int_0^{2\pi} \frac{\mathrm{d}a}{\mathrm{d}E}\mathrm{d}E \\ \quad = -a^2 k\rho \int_0^{2\pi} (1 + 2e\cos E + O(e^2))\mathrm{d}E \approx -2\pi a^2 k\rho, \\ \Delta e = \int_0^{2\pi} \frac{\mathrm{d}e}{\mathrm{d}E}\mathrm{d}E = -a(1-e^2)k\rho \\ \quad \cdot \int_0^{2\pi} \left(\cos E + \frac{1}{2}e(1+\cos(2E)) + O(e^2) \right)\mathrm{d}E, \\ \Delta \tilde{M} = \int_0^T n\mathrm{d}t - 2\pi \\ \quad = \int_0^T \left(n_0 - \frac{3}{2}n_0 \frac{\dot{a}}{a_0} t \right)\mathrm{d}t - 2\pi = -\frac{3}{2}\pi\frac{\Delta a}{a} \approx 3\pi^2 ak\rho, \end{cases} \tag{5}$$

where $T = 2\pi\sqrt{a^3/\mu}$ is the orbital period, a_0 is the initial semimajor axis, and n_0 is the initial orbital rate. $\Delta\omega$ and ΔM^* are zero because the integrands $\mathrm{d}\omega/\mathrm{d}E$ and $\mathrm{d}M^*/\mathrm{d}E$ are both odd functions. $\Delta\tilde{M}$ is brought in because the orbital angular velocity increases because of the gradual orbital decay.

It is obvious that Δe=0 if the eccentricity is zero. However, for the real space environment, orbital eccentricity cannot be precisely zero. The final eccentricity will deviate from the initial one if the satellite area–mass ratio changes within one cycle. Then it will influence the relative radial motion, which needs extra consideration.

When the eccentricity is small enough, the perturbation equation can be described approximately as follows:

$$\frac{\mathrm{d}e}{\mathrm{d}E} = -ak\rho\cos E. \tag{6}$$

Thus, the satellite eccentricity variation can be integrated as

$$\begin{aligned} \Delta e &= \int_{E_0}^{E_0+nt} -ak\rho\cos E\mathrm{d}E \\ &= -ak\rho[\sin(E_0+nt) - \sin E_0]. \end{aligned} \tag{7}$$

3.3 Nonlinear optimization for formation control

As previously stated, the derivative of the semimajor axis decreasing with respect to time for the nearly circular orbit is $\frac{\mathrm{d}a}{\mathrm{d}t} = \frac{\Delta a}{T} = -\sqrt{\mu a}k\rho$. Then the change rate of the difference between two semimajor axes is

$$\Delta\left(\frac{\mathrm{d}a}{\mathrm{d}t}\right) = -\sqrt{\mu a}\Delta k\rho. \tag{8}$$

According to Eq. (5), the in-track drift acceleration can be derived as

$$\begin{aligned} \Delta\left(\frac{\mathrm{d}^2 s}{\mathrm{d}t^2}\right) &= \Delta\left(\frac{\mathrm{d}n}{\mathrm{d}t}\right)a = \Delta\left(\frac{\mathrm{d}n}{\mathrm{d}a}\frac{\mathrm{d}a}{\mathrm{d}t}\right)a \\ &= -\frac{3}{2}\sqrt{\frac{\mu}{a^3}}\Delta\left(\frac{\mathrm{d}a}{\mathrm{d}t}\right) = \frac{3}{2}\frac{\mu}{a}\Delta k\rho. \end{aligned} \tag{9}$$

We can derive the relative drift of two satellites by integrating Eq. (9) over time:

$$s = \frac{1}{2}\left(\frac{\mathrm{d}^2 s}{\mathrm{d}t^2}\right)t^2 = \frac{3}{4}\frac{\mu}{a}\Delta k\rho t^2. \tag{10}$$

Here we find that the relative motion of in-track is a double integral system. To achieve the desired in-track drift distance, the area–mass ratio and mean semimajor axis are required to be equal eventually. Thus, the control law is designed as the following two steps:

Step 1: Adjust the semimajor axis difference and the orbital phase.

Adjust the cross-sectional areas and form the atmospheric drag difference first. It leads to the change of the semimajor axis difference. The in-track drift will be created through the orbital angular velocity difference.

Step 2: Eliminate the semimajor axis difference and set the orbital phase to the target.

The cross-sectional areas are adjusted again to eliminate the semimajor axis difference. The in-track relative velocity will slow down to zero until reaching the same altitude finally, where the desired formation is also achieved. Simultaneously, area–mass ratios are set equal to each other.

According to Eq. (10), the time spans of the above two steps are set as t_1 and t_2, respectively. The drag coefficients of two satellites are set as k_1 and k_2 for step 1 and k_3 and k_4 for step 2. The semimajor axis difference and drift distance in two steps are calculated as

$$\begin{aligned}&t_1:\ \begin{cases}\Delta a_1=(k_2-k_1)\sqrt{\mu a}\rho t_1,\\ s_1=\dfrac{3}{4}\dfrac{\mu}{a}(k_2-k_1)\rho t_1^2,\end{cases}\\ &t_2:\ \begin{cases}\Delta a_2=(k_4-k_3)\sqrt{\mu a}\rho t_2,\\ s_2=-\dfrac{3}{4}\dfrac{\mu}{a}(k_4-k_3)\rho t_2^2.\end{cases}\end{aligned} \tag{11}$$

To achieve the same semimajor axis and the desired in-track separation, we have

$$\begin{cases}a_2-a_1-\Delta a_1-\Delta a_2=0,\\ s_{\rm d}-\Delta u_0\cdot r_0-s_1-s_2=0,\end{cases} \tag{12}$$

where a_1 and a_2 are the initial semimajor axis of satellite A (Sat-A) and Sat-B, respectively, $s_{\rm d}$ is the desired in-track separation, Δu_0 is the initial argument of the latitude difference between two satellites, and r_0 is the initial geocentric distance. Thus, $\Delta u_0 \cdot r_0$ represents the initial in-track separation.

Next, an MNLP (Bazaraa *et al.*, 2013) is designed to take orbit eccentricity into consideration. Define $\boldsymbol{k}=[k_1, k_2, k_3, k_4]$ and $\boldsymbol{t}=[t_1, t_2]$. Then the constraint optimization objective function can be designed as

$$\min\ \begin{cases}f_1(\boldsymbol{k},\boldsymbol{t})=|e_1+\Delta e_1|,\\ f_2(\boldsymbol{k},\boldsymbol{t})=|e_2+\Delta e_2-e_1-\Delta e_1|.\end{cases} \tag{13}$$

According to the relative kinematic equation of the satellite, radial motion $x(f)$ and in-track motion $y(f)$ can be expressed through the orbit elements (Schaub and Alfriend, 2002) as

$$\begin{cases}x(f)\approx\dfrac{r}{a}\delta a-a\cos f\cdot\delta e+\dfrac{ae\sin f}{(1-e^2)^{1/2}}\delta M,\\ y(f)\approx\dfrac{r(1+e\cos f)^2}{(1-e^2)^{3/2}}\delta M+r\delta\omega\\ \qquad+\dfrac{r\sin f\cdot(2+e\cos f)}{1-e^2}\delta e+r\cos i\cdot\delta\Omega,\end{cases} \tag{14}$$

where δM is relative to the desired in-track separation. When $\delta a=0$, at the final moment, the amplitudes of radial and in-track motions will decrease if e and δe get smaller. Thus, the objective function f_1 is to minimize the eccentricity of the chief satellite, and f_2 is to minimize the eccentricity difference between the two satellites.

Finally, the entire optimization problem is set as

$$\begin{aligned}&\min f_1(\boldsymbol{k},\boldsymbol{t})+f_2(\boldsymbol{k},\boldsymbol{t})\\ \text{s.t.}\ \ &a_2-a_1-\Delta a_1-\Delta a_2=0,\\ &s_{\rm d}-\Delta u_0\cdot r_0-s_1-s_2=0,\\ &t_1,t_2>0,\\ &A_{11},A_{12},A_{21},A_{22}\in[A_{\min},A_{\max}],\\ &|A_{11}-A_{21}|,\ |A_{12}-A_{22}|\geq\Delta A_{\min},\end{aligned} \tag{15}$$

where A_{ij} (i, j=1, 2) are the cross-sectional areas of two satellites before and after attitude adjustment, $\Delta A_{\min}$ is the actual achievable minimum cross-sectional area difference between two satellites, which is limited by attitude control precision, and $A_{\min}$ and $A_{\max}$ are the actual achievable minimum and maximum cross-sectional areas under the structure constraint, respectively.

One important thing to note is that the mean orbit elements should be chosen to calculate the above equations, so that the instantaneous gravitational perturbation influence can be eliminated.

4 Cross-sectional area adjustment algorithm

ZJUCubeSat's attitude control system has a bias momentum wheel and magnetic coils as actuators. There are mainly two control modes: pitch maneuver mode and Earth stabilization mode. In the pitch maneuver mode, since the pitch attitude is decoupled with roll-yaw attitude, only the bias momentum wheel is needed for pitch attitude adjustment. In the Earth stabilization mode, the momentum wheel provides the bias momentum along the pitch axis, and magnetic coils are used to achieve three-axis attitude control.

4.1 Desired attitude calculation

For a satellite with a cubic structure (Fig. 3), set a, b, and c as the length of the sides that correspond to the rolling axis (x), pitch axis (y), and yaw axis (z), respectively. Thus, the surface areas can be calculated as $A_1=A_4=bc$, $A_2=A_5=ac$, and $A_3=A_6=ab$.

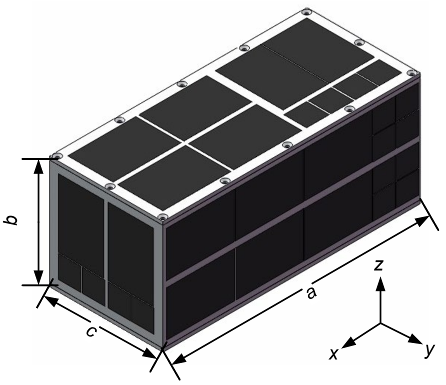

Fig. 3 Three-dimensional sizes of ZJUCubeSat

Setting the satellite attitude angles as φ (roll angle), θ (pitch angle), and ψ (yaw angle), the cross-sectional area can be derived as

$$\begin{aligned}A=\sum_{i=1}^{6}A_{i,\text{effect}}&=A_1\left|\cos\theta\cos\psi-\sin\theta\sin\phi\sin\psi\right|\\&+A_2\left|-\cos\phi\sin\psi\right|+A_3\left|\sin\theta\cos\psi+\cos\theta\sin\psi\sin\phi\right|,\end{aligned}\tag{16}$$

where $A_{i,\text{effect}}$ (i=1, 2, …, 6) means the effective cross-sectional area for each surface.

When calculating the desired pitch angle, the desired roll and yaw angles are set as zero, and thus Eq. (16) can degenerate to the following type:

$$A=\sum_{i=1}^{6}A_{i,\text{effect}}=A_1\left|\cos\theta\right|+A_3\left|\sin\theta\right|.\tag{17}$$

Setting the desired cross-sectional area as A_d, the formula is derived to calculate the desired pitch angle:

$$\theta_\text{d}=\text{sgn}(\theta_0)\left[\text{asin}\left(\frac{A_\text{d}}{A_1^2+A_3^2}\right)-\text{atan}\left(\frac{A_1}{A_3}\right)\right].\tag{18}$$

For the same desired area, two equal pitch angles but with different signs both satisfy the requirement, which coincides with the fact. The sign of the current pitch angle, sgn(θ_0), is selected to minimize the rotation range and reduce the maneuvering time. Thus, the desired attitude quaternion is derived as $\boldsymbol{q}_\text{d}$=[0, sin(0.5θ_d), 0, cos(0.5θ_d)].

4.2 Three-axis stabilization control law

Magnetic coils are used during the three-axis stabilization mode, and the PD control law is set as follows:

$$\boldsymbol{T}_\text{c}=-\boldsymbol{K}_\text{p}\boldsymbol{q}_\text{e}\,\text{sgn}(q_{\text{e},4})-\boldsymbol{K}_\text{d}\boldsymbol{\omega}_\text{e},\tag{19}$$

where $\boldsymbol{K}_\text{p}$ and $\boldsymbol{K}_\text{d}$ are the feedback gain matrices, $\boldsymbol{q}_\text{e}$ and $\boldsymbol{\omega}_\text{e}$ are the attitude error quaternion and angular velocity offset, respectively, $q_{\text{e},4}$ is the scalar part of the error quaternion, and $\boldsymbol{T}_\text{c}$ is the ideal output torque.

Transition between the ideal and actual output torques is

$$\boldsymbol{m}=\boldsymbol{B}_\text{b}\times\boldsymbol{T}_\text{c}\Big/\left\|\boldsymbol{B}_\text{b}\right\|^2,\tag{20}$$

where $\boldsymbol{B}_\text{b}$ is the Earth's magnetic field vector measured in the body coordinate system.

4.3 Pitching maneuver control law

When the three-axis attitude angles are stable, a nonlinear PD control law is designed to implement pitch attitude maneuver using the bias momentum wheel:

$$\boldsymbol{T}_\text{c}=-\boldsymbol{K}_\text{pw}\boldsymbol{q}_{\text{e},2}\big/q_{\text{e},4}-\boldsymbol{K}_\text{dw}\boldsymbol{\omega}_{\text{e},2},\tag{21}$$

where $\boldsymbol{K}_\text{pw}$ and $\boldsymbol{K}_\text{dw}$ are the feedback gain matrices, and $\boldsymbol{q}_{\text{e},2}$ and $\boldsymbol{\omega}_{\text{e},2}$ are the attitude error quaternion and angular velocity offset of the pitch axis, respectively. If $q_{\text{e},4}$ is small (i.e., the attitude angle error is large), the damping rate of the system is relatively small and the attitude maneuver speed increases rapidly. Until the attitude error recovers to a small level, the damping rate of the system increases and the angular velocity gradually converges to zero.

4.4 Actuator constraint design

The bias momentum wheel has a saturation issue. The maximum torque generated by the wheel is limited due to the motor speed-regulating capacity. The optimal design should be considered to satisfy these actuator constraints.

We set the maximum angular momentum of momentum wheel as h_max, and the maximum angular momentum variation provided by the motor as Δh_max. Thus, the maximum actuating angular rate that the satellite can achieve will be $\omega_{\text{e,max}}=h_\text{max}/J_2$, where J_2 is the moment of inertia of the pitch axis. The output torque should decrease to zero with the momentum wheel gradually reaching the maximum rotating speed or the permissible minimum rotating speed, to provide the necessary bias momentum. As seen from Eq. (21), the output torque just crosses zero when the actuating rate reaches the maximum:

$$\boldsymbol{K}_{\mathrm{p}}\boldsymbol{q}_{\mathrm{e},2} / q_{\mathrm{e},4} + \boldsymbol{K}_{\mathrm{d}}\boldsymbol{\omega}_{\mathrm{e},2} = \boldsymbol{0}. \tag{22}$$

After simplification, the maximum permissible attitude error quaternion can be derived as follows:

$$q_{\mathrm{emax}} = \min\left(K_{\mathrm{d}}(i,i) q_{\mathrm{e}0,4} \omega_{\mathrm{emax}} / K_{\mathrm{p}}(i,i)\right),\ i=1,2,3, \tag{23}$$

where $q_{\mathrm{e}0,4}$ is the scalar part of the initial error quaternion. We set the vector part of the initial error quaternion as $\boldsymbol{\varepsilon}$. Thus, we can calculate the error quaternion that generates into the control algorithm each time:

$$\begin{aligned} &\bar{\boldsymbol{q}}_{\mathrm{e}} = \begin{cases} \boldsymbol{q}_{\mathrm{e}}, & \max\left(|\boldsymbol{\varepsilon}|\right) \le q_{\mathrm{e\,max}}, \\ K_{\mathrm{q}}\boldsymbol{q}_{\mathrm{e}}, & \max\left(|\boldsymbol{\varepsilon}|\right) > q_{\mathrm{e\,max}}, \end{cases} \\ &K_{\mathrm{q}} = q_{\mathrm{e\,max}} \big/ \max\left(|\boldsymbol{\varepsilon}|\right). \end{aligned} \tag{24}$$

Considering the motor speed-regulating constraint, the final output torque is calculated as follows:

$$\begin{aligned} &\bar{\boldsymbol{T}}_{\mathrm{c}} = \begin{cases} \boldsymbol{T}_{\mathrm{c}}, & \max\left(|\boldsymbol{T}_{\mathrm{c}}|\right) \le \Delta h_{\max}, \\ K_{\mathrm{T}}\boldsymbol{T}_{\mathrm{c}}, & \max\left(|\boldsymbol{T}_{\mathrm{c}}|\right) > \Delta h_{\max}, \end{cases} \\ &K_{\mathrm{T}} = \Delta h_{\max} \big/ \max\left(|\boldsymbol{T}_{\mathrm{c}}|\right). \end{aligned} \tag{25}$$

Fig. 4 shows the entire formation control logic diagram, which can be applied in practice. In the first place, the on-board GPS receiver will help obtain the mean orbit elements and analyze the coefficients used in the atmosphere model. Because of the fact that the nonlinear programming method is very complicated and the calculation capacity of the CubeSat's on-orbit computer is limited, the MNLP method will be used to calculate the desired cross-sectional areas and desired attitudes on the ground. Then the hold times t_1, t_2 and the desired pitch attitudes $\theta_{\mathrm{d}1}$, $\theta_{\mathrm{d}2}$ will be relayed to the corresponding satellites through the ground station. At the end of t_2, the formation is achieved and the attitude will be switched to the three-axis Earth-pointing stabilization mode for reducing the orbital decay rate and starting the inter-satellite ranging experiment. If the final relative motion condition is not very stable due to the atmospheric modeling error, the above process is again used to revise the relative motion.

5 Numerical simulation

In this section, numerical simulations are presented to verify the above strategy using the parameters of ZJUCubeSat. The initial orbit height is 300 km. The initial mean semimajor axis difference is 0.008 km, and the mean anomaly difference is −0.0008°. Thus, the distance between two satellites is roughly 100 m at the beginning. The initial attitude angle is set as [0, 0, 0]°, and the initial angular velocity is [0, 0, 0]°/s in the orbit coordinate system. The satellite parameters and actuator configurations are shown in Table 1. Hence, the pitch attitude maneuver could generate a cross-sectional area ranging from $A_{\min}$=0.01 m^2 to $A_{\max}$=0.0248 m^2.

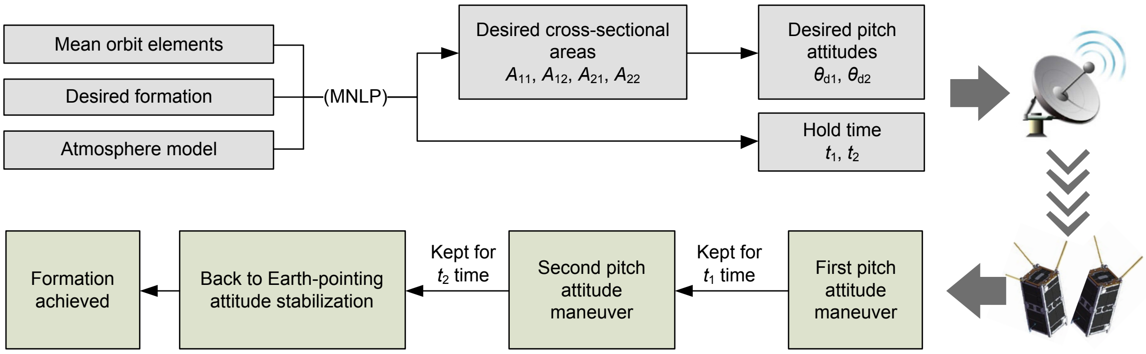

Fig. 4 Top-level multidimensional nonlinear constraint programming (MNLP) formation control logic

Table 1 Configuration of orbit parameters and attitude control actuators

Orbit parameter	Mean value		Parameter	Value
	Sat-A	Sat-B		
Semimajor axis (km)	6678.139	6678.147	Satellite inertia moment (kg·m^2)	diag(0.0033, 0.0103, 0.0103)
			Structure parameter (m)	0.2271(x)×0.1(y)×0.1(z)
Eccentricity	0.0005	0.0005	Mass (kg)	3
			Remanence (A·m^2)	[0.01, 0.01, 0.01]
Inclination (degree)	79	79	Deviation of mass center (m)	[0, 0, 0.1]
			Inertia moment of wheel (kg·m^2)	2.4e−6
Argument of perigee (degree)	0	0	Nominal speed (r/min)	8000
			Maximum speed regulation rate (r/(min·s))	400
RAAN (degree)	0	0	Maximum wheel speed (r/min)	10 000
			Minimum wheel speed (r/min)	6000
Mean anomaly (degree)	30.0000	29.9992	Magnetic moment of coils (A·m^2)	[0.14, 0.14, 0.14]
			Pitch maneuver control parameter	K_{pw}=0.0021, K_{dw}=0.0103
			Three-axis stable control parameter	$\boldsymbol{K}_{\text{p}}$=[5.73e−5, 5.73e−5, 5.73e−5] $\boldsymbol{K}_{\text{d}}$=[7e−3, 1.23e−2, 1.23e−2]

Fig. 5 shows the amount of pitch angle adjustment at different cross-sectional areas. When the minimum area difference $\Delta A_{\min}$ is small, say 0.0001 m^2, the adjustment amount is below 1° most of the time, which is beyond the attitude adjustment capacity. When the angle increases to at least 4° or even more, however, $\Delta A_{\min}$ reaches over 0.01 m^2. Thus, considering the attitude control accuracy, $\Delta A_{\min}$ is set as 0.002 m^2 for nonlinear programming. In the following numerical simulation, the interior-point algorithm (Byrd *et al.*, 1999) is applied in MATLAB to calculate the programming result, and the result will be compared with that of general BB control (Yao *et al.*, 2010).

An empirical global Earth's atmosphere model NRLMSISE-00 (Picone *et al.*, 2002) is applied in the following simulation. This model takes F10.7 solar flux and the geomagnetic activity into account. It is based on earlier models MSIS-86 and MSISE-90, and is updated with actual satellites' drag data. The inputs for the model include mainly the time, the geodetic coordinates, and also the solar and magnetic data.

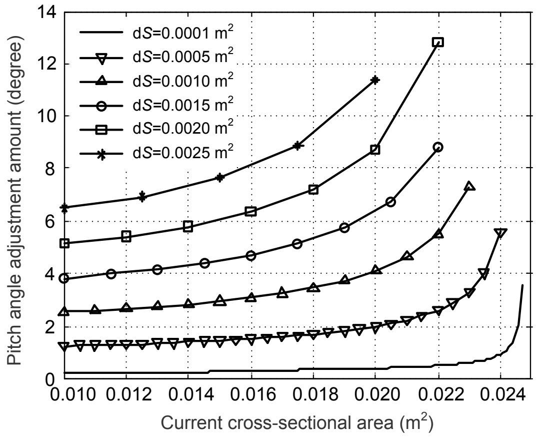

Fig. 5 Pitch angle adjustment amount at a certain cross-sectional area

The value of 2.2 has been widely used as the drag coefficient C_{d} for all satellites with a compact shape. However, the drag coefficient can take different values depending on the spacecraft's shape, surface material, and the atmospheric temperature and composition. Schamberg (1959) proposed a general model of gas-surface interaction. Assuming that the remission of atmospheric molecules is mainly diffusive because the satellite surface is fairly cool, the approximation of C_{d} for the flat plate is (Gaposchkin, 1994)

$$C_{\text{d},i} = 1 + \frac{2}{3}\sqrt{1 + \alpha_i\left(\frac{T_{\text{w},i}}{T_{\text{a}}} - 1\right)}\cos\theta_i, \tag{26}$$

where $C_{\text{d},i}$ is the coefficient of drag for each surface, $T_{\text{w},i}$ is the temperature of each plate, and T_{a} is the temperature of the atmosphere. θ_i is the angle of the incident gas flow with respect to each plate. α_i is the accommodation coefficient and has the following approximation:

$$\alpha_i = \frac{3.6\mu_i}{(1+\mu_i)^2}, \tag{27}$$

where μ_i is the ratio of the mass of the incident gas atom to the mass of the surface atom. For a glass surface (solar cell protection), α_i is chosen as 0.73

(Moe and Moe, 2005). Thus, the drag coefficient can be calculated according to the actual satellite attitude.

To indicate the influence of the drag coefficient estimation bias on the formation accuracy, C_d is set as 2.20 in MNLP calculation, while the real drag coefficient is set as 2.12 to 2.24 during orbit propagation. Fig. 6 shows the variation tendency of the 1000-m in-track formation. It affects mainly the orbital decay rate and generates a small difference between the final mean semimajor axes of two satellites. In a practical application, considering that C_d is very important for calculating the drifting time and that the above model is still not accurate enough, C_d will be estimated through the GPS orbit determination data beforehand for more precise control.

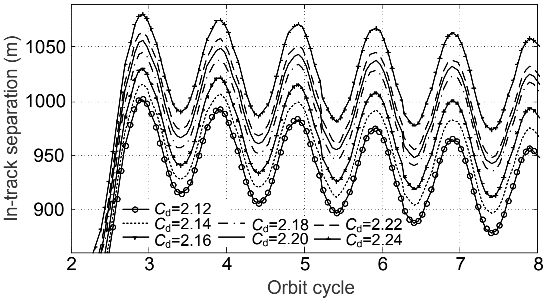

Fig. 6 Influence of the drag coefficient on the formation accuracy

In addition, the velocity of the atmosphere is approximately the same as the Earth's rotation velocity in the above MNLP strategy. However, atmospheric wind is not negligible in the orbit. An empirical model HWM07 (Drob *et al.*, 2008) provides a statistical representation of the Earth's horizontal wind fields, which will be adopted in the following simulation. Fig. 7 shows the influence of horizontal wind on the formation accuracy.

If the horizontal wind is ignored, the in-track separation drifts much more slowly after the configuration has been formed due to the consideration of the atmosphere's co-rotation around the Earth. However, the horizontal wind has impact on the relative velocity between the atmosphere and the satellite, which will cause the orbital decay rate not to coincide with the expectation. The final mean semimajor axes of two satellites may have a little difference, leading to the separation drifting with time.

Considering that the model is much more complex and that the horizontal wind is only tens of meters most of the time, while the atmosphere's co-rotation velocity is approximately 486 m/s in the 300-km orbit height, the horizontal velocity is not considered in the MNLP strategy. Thus, in the practical operation, if necessary, the semimajor axes should have slight modifications through several adjustments.

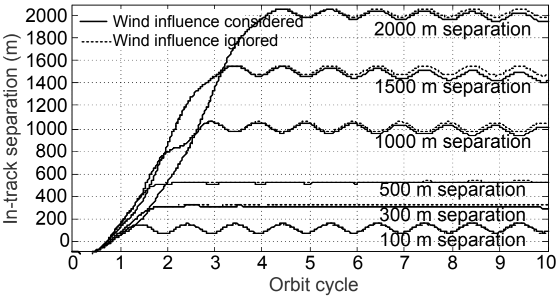

Fig. 7 Influence of horizontal wind on the formation accuracy using the HWM07 model

5.1 In-track drifting simulation results

The desired in-track separation S_d is set as 500 and 1500 m. Table 2 lists the cross-sectional areas and hold times of Sat-A and Sat-B derived from MNLP control. For BB control, the cross-sectional areas are set as 0.0248 and 0.01 m^2, respectively. The orbital period is about 5430 s for a 300-km near-circular orbit. Thus, a 500-m separation distance could be achieved for about two orbit cycles and a 1500 m separation for about 3.5 orbit cycles.

Fig. 8 presents the variation tendency of the semimajor axes. In the initial phase, the orbit altitude of Sat-B is higher, and after the adjustment during t_1 and t_2 time, the orbit altitudes of both satellites arrive at nearly the same value. The detailed view shows that the differences between the two semimajor axes are all within 1 m, which can mostly satisfy the formation requirement. The primary cause of the control deviation is that the atmospheric model used in the MNLP method is a static one, which shows the variation tendency of the atmosphere clearly and is convenient for derivation and computation. However, the NRLMSISE-00 model used in the simulation is a time-varying one and is influenced by many factors, which brings more semimajor axis deviation for the long formation adjustment time.

Table 2 Cross-sectional areas and hold times to achieve in-track formation

In-track separation	Time (s)		Cross-sectional area (m^2)			
	NPC	BBC	NPC		BBC	
			Sat-A	Sat-B	Sat-A	Sat-B
500 m	t_1=5724	t_1=5822	0.0100	0.0219	0.0100	0.0248
	t_2=6029	t_2=5195	0.0241	0.0100	0.0248	0.0100
1500 m	t_1=10 573	t_1=9122	0.0100	0.0248	0.0100	0.0248
	t_2=8028	t_2=8495	0.0219	0.0100	0.0248	0.0100

NPC: nonlinear programming control; BBC: Bang-Bang control

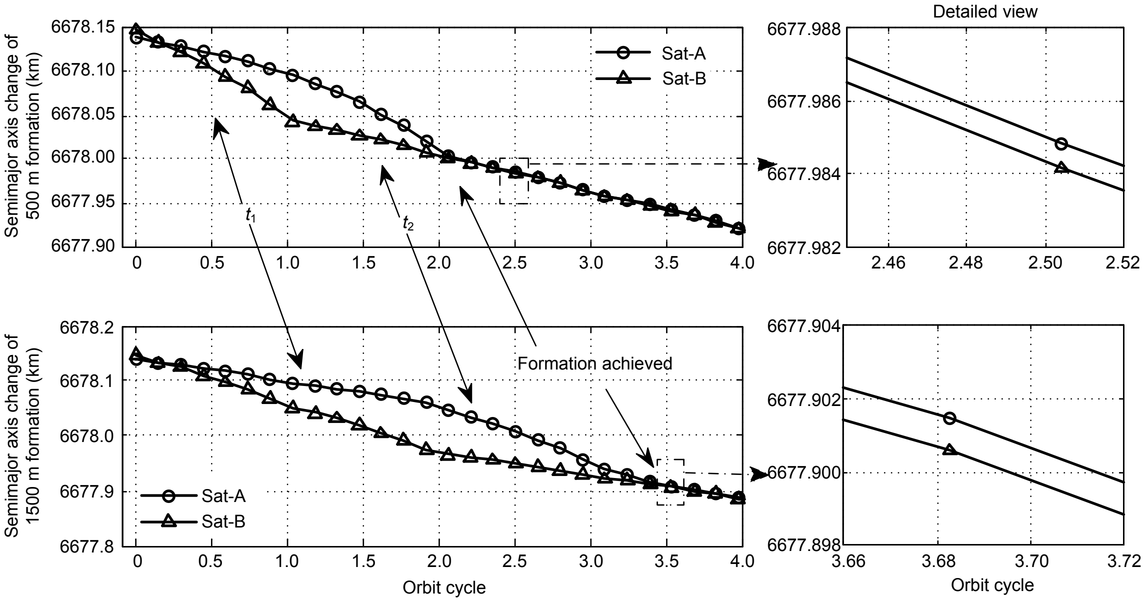

Fig. 8 Variation tendency of the semimajor axis during the formation of the configuration

Next, we compare MNLP control and BB control in 500- and 1500-m in-track formation simulations. As shown in Fig. 9 (right) and Fig. 10 (right), the final eccentricities and final eccentricity differences of two satellites are both smaller in MNLP control, which are due to the consideration of the drag influence on eccentricity. According to Eq. (14), the in-track and radial oscillations would also be smaller. Fig. 9 (left) and Fig. 10 (left) show these expected outcomes. We can see that the separation between the two satellites is not consistent with expectations very much, and the separation drifts slowly. The main reason is that the zonal wind and meridional wind are ignored in the atmospheric model that the MNLP method uses. The time variation of the atmosphere also contributes to the drift.

Finally, Table 3 lists the elapsed time and the standard deviations of the in-track and radial oscillation amplitudes of two control algorithms for multiple in-track formation simulations. We can see that the formation precision has a very significant effect when using MNLP control, while the elapsed time increases only a little more than that of BB control.

Additionally, it needs to be emphasized that the above simulation accuracies hold only for the simplified model condition but will decrease in the real space environment. It is because the models used in the simulation, namely the NRLMSISE-00 atmospheric model and HWM07 horizontal wind model, are both empirical and time-varying. All the density models have similar 1-sigma errors of about 15% (Marcos, 2006). Vallado and Finkleman (2014) listed the major error sources in using atmospheric models. Furthermore, orbit determination and drag coefficient estimation introduce errors in the MNLP method. Figs. 6 and 7 indicate some impacts of these errors on MNLP calculation results.

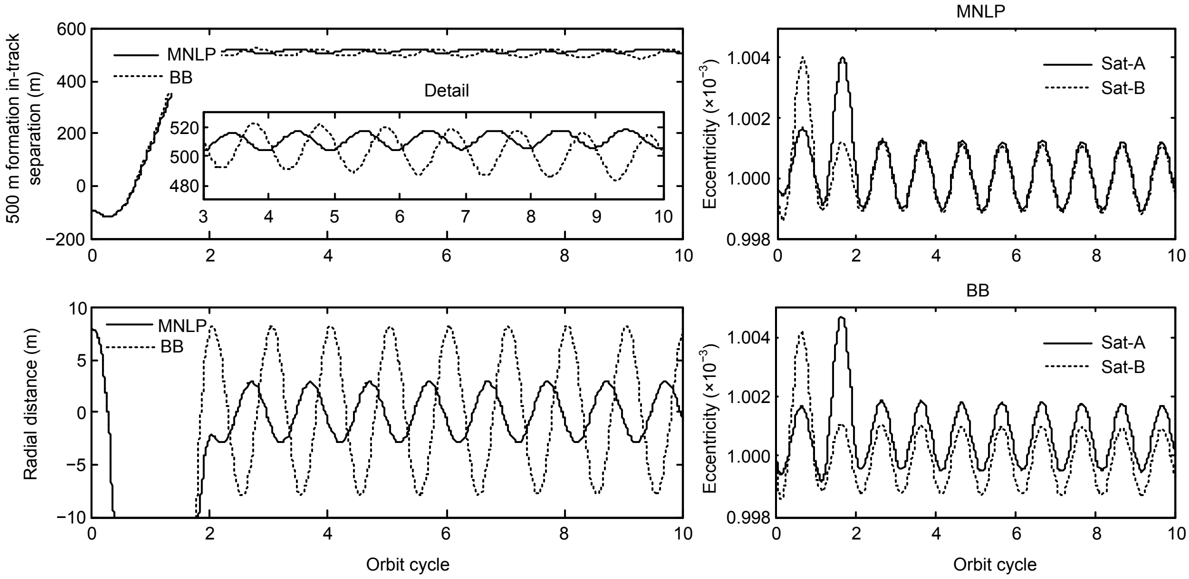

Fig. 9 The 500 m formation comparison of two control algorithms MNLP and BB

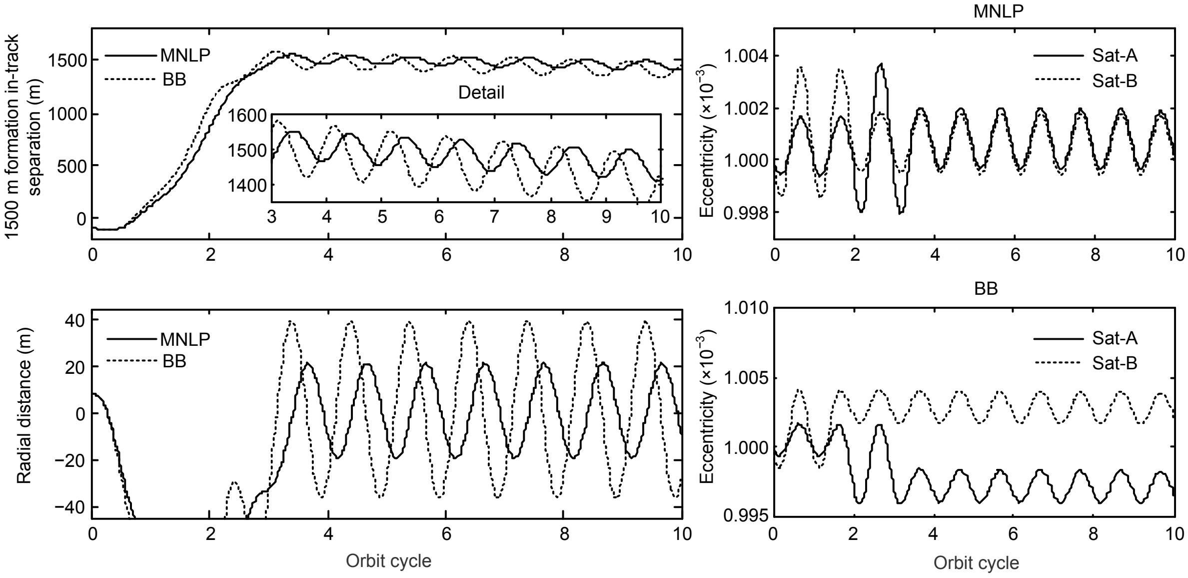

Fig. 10 The 1500 m formation comparison of two control algorithms MNLP and BB

Table 3 Relative motion oscillation and elapsed time comparison of two control algorithms

In-track formation separation (m)	In-track (std. (m))		Radial (std. (m))		Elapsed time (orbit cycle)	
	MNLP	Bang-Bang	MNLP	Bang-Bang	MNLP	Bang-Bang
100	28.559	55.121	14.229	27.586	1.41	1.22
200	28.808	38.794	13.348	17.589	1.54	1.47
300	2.463	18.288	0.525	8.046	2.16	1.68
500	5.526	9.054	1.714	5.369	2.16	2.03
1000	29.035	49.399	15.769	25.721	3.17	2.71
1500	29.570	56.582	14.394	27.731	3.43	3.24
5000	4.847	13.692	1.440	3.984	6.17	5.70

5.2 Cross-sectional area control simulation results

Here we take 500-m in-track formation attitude control as an example. As seen from Table 2, the cross-sectional areas 0.0219 and 0.0241 m^2 correspond to the desired pitch attitude angle 38.19° and 52.45°, respectively, calculated through Eq. (18). Figs. 11 and 12 show the variation tendencies of the three-axis attitude angle, cross-sectional area, and bias momentum wheel speed of Sat-A and Sat-B.

At the beginning, the attitude is in a relatively stable state, and the bias momentum wheel starts to regulate speed for large-scale attitude maneuver when the time of t_1 or t_2 is up. Then, magnetic coils are used for subsequent stable control. In less than 50 s, the pitch attitude is much close to the target and hovers around the reference pitch angle eventually. After the formation has been achieved, both satellites change to the three-axis Earth-pointing attitude for formation maintenance. From data analysis, the pitch angle fluctuations are both less than 2°, and have the accuracies of 1.547° (3σ) for Sat-A and 1.07 8° (3σ) for Sat-B. The roll angle and yaw angle hover around 0° with accuracies of 1.205° (3σ) and 0.735° (3σ) for Sat-A, and accuracies of 0.910° (3σ) and 0.931° (3σ) for Sat-B. Attitude control precision can be kept only at this level because of the control actuators constraint and the low Earth orbit disturbing torques.

Correspondingly, the cross-sectional areas of both satellites achieve the target for a short time, and then hover around it with accuracies of 3.33 cm^2 (3σ) for Sat-A and 2.90 cm^2 (3σ) for Sat-B. At this level, the atmospheric drag offset is small enough, which can satisfy the mission requirement. During pitch attitude maneuver, the speed of the bias momentum wheel is constrained within the maximum and minimum speed requirements, which illustrates the validity of controller saturation constraint design.

6 Conclusions

After presenting the ZJUCubeSat mission, we have presented the design of an integrated control strategy for low-Earth-orbit CubeSats to achieve the desired in-track formation through atmospheric drag. A multidimensional nonlinear constraint programming (MNLP) strategy was designed to calculate different desired area–mass ratios and relevant hold times for orbit adjustment, which takes both the mean semimajor axis and mean eccentricity into account. A nonlinear PD controller was designed to adjust the

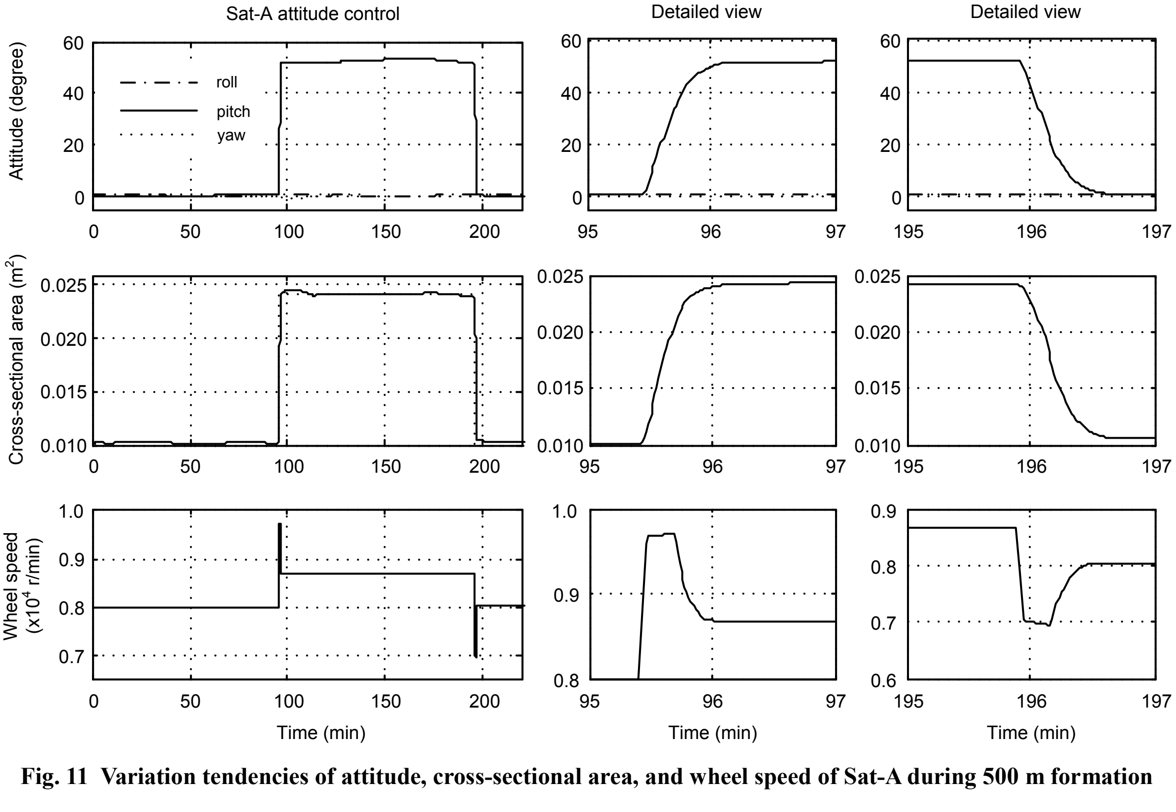

Fig. 11 Variation tendencies of attitude, cross-sectional area, and wheel speed of Sat-A during 500 m formation

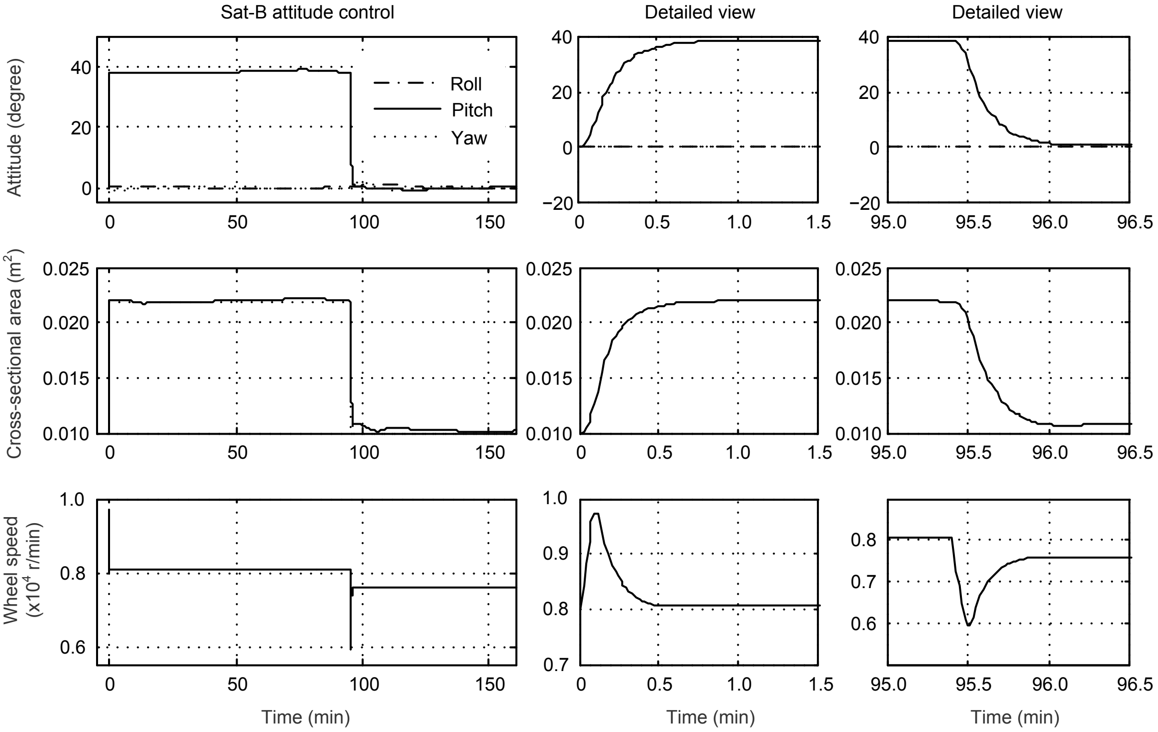

Fig. 12 Variation tendencies of attitude, cross-sectional area, and wheel speed of Sat-B during 500 m formation

satellite area–mass ratio by changing pitch attitude via a bias momentum wheel, which could realize fast and large-scale attitude maneuver and pitch axis stability control. Then the normal PD controller used magnetic coils to maintain three-axis stabilization. Numerical simulation based on the 3-kg ZJUCubeSat analyzed the adverse effect of the modeling inaccuracies and verified the feasibility and advantage of the design. Furthermore, the attitude control algorithm is much simpler and can be achieved through the general actuator configuration. The entire strategy will be implemented in the inter-satellite ranging experiment of ZJUCubeSat. It can also be applied to other CubeSats that cannot configure the propulsion system or a deployable mechanism. It helps reduce the satellite flexible vibration, payload mass, and power consumption, and extends the application of CubeSats. On account of the variability of the real atmospheric state, further work will be concentrated on the reduction of the coefficient estimation error and the enhancement of control stability and accuracy. Also, a simple and effective algorithm based on this MNLP method will be designed to accommodate to automatic on-board computing, which will be more convenient and more accurate than the present satellite–ground open-loop control.

References

Bazaraa, M.S., Sherali, H.D., Shetty, C.M., 2013. Nonlinear Programming: Theory and Algorithms. John Wiley & Sons, New Jersey.

Byrd, R.H., Hribar, M.E., Nocedal, J., 1999. An interior point algorithm for large-scale nonlinear programming. *SIAM J. Optim.*, **9**(4):877-900. https://doi.org/10.1137/S1052623497325107

Cai, B., Wang, H., Zhu, X., *et al.*, 2011. Design of the Earth magnetic field measurement system for pico-satellites. *Chin. J. Sens. Actuat.*, **27**(8):1-5 (in Chinese). https://doi.org/10.3969/j.issn.1004-1699.2011.08.026

Campbell, M., Fullmer, R.R., Hall, C.D., 2000. The ION-F formation flying experiments. AAS/AIAA Space Flight Mechanics Meeting, p.135-149. https://doi.org/10.13140/2.1.3903.3603

Drob, D., Emmert, J., Crowley, G., *et al.*, 2008. An empirical model of the Earth's horizontal wind fields: HWM07. *J. Geophys. Res. Space Phys.*, **113**:A12304. https://doi.org/10.1029/2008JA013668

Eyer, J.K., Damaren, C.J., Zee, R.E., *et al.*, 2007. A formation flying control algorithm for the CanX-4&5 low Earth orbit nanosatellite mission. *Space Technol.*, **27**(4):147-158.

Gaposchkin, E.M., 1994. Calculation of Satellite Drag Coefficients. Technical Report, DTIC Document.

Horsley, M., Nikolaev, S., Pertica, A., 2013. Small satellite rendezvous using differential lift and drag. *J. Guid. Contr. Dynam.*, **36**(2):445-453.

https://doi.org/10.2514/1.57327

Lambert, C., Kumar, B.S., Hamel, J.F., *et al*., 2012. Implementation and performance of formation flying using differential drag. *Acta Astronaut.*, **71**:68-82. https://doi.org/10.1016/j.actaastro.2011.08.013

Leonard, C.L., Hollister, W.M., Bergmann, E.V., 1989. Orbital formationkeeping with differential drag. *J. Guid. Contr. Dynam.*, **12**(1):108-113. https://doi.org/10.2514/3.20374

Liu, L., 2000. Orbit Theory of Spacecraft. National Defense Industry Press, Beijing, p.86-90 (in Chinese).

Lohn, J.D., Hornby, G.S., Linden, D.S., 2005. An evolved antenna for deployment on NASA's Space Technology 5 Mission. *In*: O'Reilly, U.M., Yu, T., Riolo, R., *et al.* (Eds.), Genetic Programming Theory and Practice II. Springer, New York, p.301-315. https://doi.org/10.1007/0-387-23254-0_18

Marcos, F.A., 2006. New satellite drag modeling capabilities. 44th AIAA Aerospace Sciences Meeting and Exhibit, p.1-13. https://doi.org/10.2514/6.2006-470

Meng, T., Wang, H., Jin, Z.H., *et al*., 2009. Attitude stabilization of a pico-satellite by momentum wheel and magnetic coils. *J. Zhejiang Univ.-Sci. A*, **10**(11):1617-1623. https://doi.org/10.1631/jzus.A0820425

Moe, K., Moe, M.M., 2005. Gas–surface interactions and satellite drag coefficients. *Planet. Space Sci.*, **53**(8):793-801. https://doi.org/10.1016/j.pss.2005.03.005

Montenbruck, O., Gill, E., 2012. Satellite Orbits: Models, Methods and Applications. Springer Science & Business Media.

Pérez, D., Bevilacqua, R., 2013. Differential drag spacecraft rendezvous using an adaptive Lyapunov control strategy. *Acta Astronaut.*, **83**:196-207. https://doi.org/10.1016/j.actaastro.2012.09.005

Picone, J.M., Hedin, A.E., Drob, D.P., *et al*., 2002. NRLMSISE-00 empirical model of the atmosphere: statistical comparisons and scientific issues. *J. Geophys. Res. Space Phys.*, **107**(A12):SIA15-1-SIA15-16. https://doi.org/10.1029/2002JA009430

Reid, T., Misra, A.K., 2011. Formation flight of satellites in the presence of atmospheric drag. *J. Aerosp. Eng. Sci. Appl.*, **3**(1):64-91.

Reinhard, R., Asma, C., Muylaert, J., 2012. The QB50 project: a Network of 50 Cubesats. Von Karman Institute for Fluid Dynamics, Rhode Saint Genese, Belgium.

Schamberg, R., 1959. A New Analytic Representation of Surface Interaction for Hyperthermal Free Molecule Flow with Application to Neutral-Particle Drag Estimates of Satellites. Rand Corporation.

Schaub, H., Alfriend, K.T., 2002. Hybrid Cartesian and orbit element feedback law for formation flying spacecraft. *J. Guid. Contr. Dynam.*, **25**(2):387-393. https://doi.org/10.2514/2.4893

Vallado, D.A., 2001. Fundamentals of Astrodynamics and Applications. Springer Science & Business Media, Berlin.

Vallado, D.A., Finkleman, D., 2014. A critical assessment of satellite drag and atmospheric density modeling. *Acta Astronaut.*, **95**:141-165. https://doi.org/10.1016/j.actaastro.2013.10.005

Varma, S., Kumar, K.D., 2012. Multiple satellite formation flying using differential aerodynamic drag. *J. Spacecr. Rock.*, **49**(2):325-336. https://doi.org/10.2514/1.52395

Wang, J., Wang, H., Ying, P., *et al*., 2012. Design of four-quadrant analog Sun sensor. *Chin. J. Sens. Actuat.*, **25**(12): 1659-1663 (in Chinese). https://doi.org/10.3969/j.issn.1004-1699.2012.12.007

Yang, M., Wang, H., Wu, C.J., *et al*., 2012. Space flight validation of design and engineering of the ZDPS-1A pico-satellite. *Chin. J. Aeronaut.*, **25**(5):725-738. https://doi.org/10.1016/S1000-9361(11)60439-1

Yao, H., Zeng, G.Q., Hu, M., 2010. Time-optimal aerodynamic control for along-track separation of spacecraft formation flying. *J. Acad. Equip. Comm. Technol.*, **21**(1):70-73 (in Chinese). https://doi.org/10.3783/j.issn.1673-0127.2010.01.017